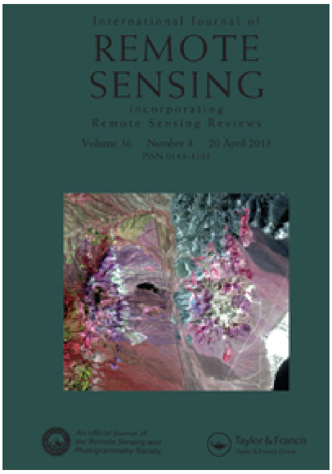

International Journal of Remote Sensing
Publication details, including instructions for authors and subscription information:
http://www.tandfonline.com/loi/tres20

Mitigating atmospheric effects in InSAR measurements through high-resolution data assimilation and numerical simulations with a weather prediction model

Ye Yun[ab], Qiming Zeng[a], Benjamin W. Green[b] & Fuqing Zhang[b]
[a] Institute of Remote Sensing and Geographic Information System, Peking University, Beijing, China
[b] Department of Meteorology, The Pennsylvania State University, University Park, Pennsylvania, USA
Published online: 20 Apr 2015.

International Journal of Remote Sensing, 2015
Vol. 36, No. 8, 2129–2147, http://dx.doi.org/10.1080/01431161.2015.1034894

Mitigating atmospheric effects in InSAR measurements through high-resolution data assimilation and numerical simulations with a weather prediction model

Ye Yun[a,b], Qiming Zeng[a]*, Benjamin W. Green[b], and Fuqing Zhang[b]

[a]*Institute of Remote Sensing and Geographic Information System, Peking University, Beijing, China;* [b]*Department of Meteorology, The Pennsylvania State University, University Park, Pennsylvania, USA*

(*Received 30 October 2014; accepted 30 January 2015*)

Repeat-pass spaceborne interferometric synthetic aperture radar (InSAR) is commonly used to measure surface deformation; phase delays due to atmospheric water vapour may have significant impact on the accuracy of these measurements. In recent years, there has been a growing interest in using forecasts and analyses from numerical weather prediction (NWP) models – which can provide good estimates of the atmospheric state – to correct for atmospheric phase delays. In this study, three separate estimates of atmospheric water vapour content from NWP output are used in combination with Environmental Satellite (Envisat) Advanced Synthetic Aperture Radar (ASAR) data over the Pearl River Delta region in South China to mitigate atmospheric distortion. The NWP-based estimates are derived from: (1) interpolation of National Centers for Environmental Prediction (NCEP) Final Operational Global Analysis (FNL) data; (2) Weather Research and Forecasting (WRF) model simulations initialized with FNL analysis without additional data assimilation; and (3) WRF simulations initialized with a three-dimensional variational (3DVar) data assimilation system that ingests additional meteorological observations. The accuracy of the atmospheric corrections from these different NWP model outputs is further verified quantitatively with precipitable water vapour (PWV) data from several ground-based global positioning system (GPS) stations in Hong Kong. Inter-comparison shows a good agreement between the PWV derived from the WRF-3DVar simulations and the GPS measurements, suggesting that atmospheric correction by convection-permitting WRF simulations initialized with mesoscale data assimilation may effectively mitigate atmospheric distortion in InSAR measurements, especially for coastal areas.

1. Introduction

Spaceborne interferometric synthetic aperture radar (InSAR) is one of the most useful methods to monitor surface movements caused by earthquakes, subsidence, and other deformations. Specifically, the repeat-pass spaceborne differential SAR interferometry (DInSAR), at different observation times, is used to detect surface deformation. However, phase delay in the atmosphere has a significant influence on the accuracy of DInSAR measurements (Hanssen 2001). Tropospheric water vapour is regarded as one of the most significant atmospheric factors affecting radar signal propagation, and will probably introduce unexpected phase changes in the interferogram (Cui et al. 2012). In some extreme cases, as Zebker, Rosen, and Hensley (1997) have shown, a 20% change in humidity can lead to errors of up to 10 cm in deformation products. Therefore, correcting

*Corresponding author. Email: qmzeng@pku.edu.cn

for the effect of tropospheric water vapour is necessary in some applications where a high level of accuracy is required.

Several methods have been applied to mitigate the atmospheric delay in InSAR data. One approach is to use multi-spectrum water vapour products such as precipitable water vapour (PWV) from the Moderate Resolution Imaging Spectroradiometer (MODIS) or the Medium Resolution Imaging Spectrometer (MERIS) (Li, Muller, et al. 2006; Zeng, Li, and Li 2007). Unfortunately this approach has several limitations: both MERIS and MODIS data are influenced by clouds and have very limited spatial coverage. There is also a large temporal gap between acquisitions of the individual MODIS sensors. Furthermore, MERIS is synchronized with the Environmental Satellite (Envisat) Advanced Synthetic Aperture Radar (ASAR), although unfortunately the Envisat satellite ceased operations in April 2012. Another approach is to integrate with dense global positioning system (GPS) networks (Williams, Bock, and Fang 1998; Li, Fielding, et al. 2006), although there are often sparse observations of GPS data. Time-series InSAR techniques such as Persistent Scatterer InSAR (Ferretti, Prati, and Rocca 2000) have also been used, but require a large number of SAR images (which may not be available for a given geographic region and period of interest (Foster et al. 2006)). A final class of mitigation methods incorporates numerical weather prediction (NWP) models (Foster et al. 2013; Gong et al. 2013; Liu, Hanssen, and Mika 2009; Mateus et al. 2009; Puysségur, Michel, and Avouac 2007; Wadge et al. 2002, 2010). Nevertheless, none of these approaches – or any combination thereof – is presently operational.

The InSAR community has recently taken great interest in NWP models because these can determine the water vapour content at the same time as SAR acquisitions (for atmospheric delay prediction), regardless of weather conditions or geographic location. Several promising results based on high-spatial resolution weather models, including the Fifth-Generation Pennsylvania State University/National Center for Atmospheric Research Mesoscale Model (MM5) and the Weather Research and Forecasting (WRF) model, can be found in the literature (Liu, Hanssen, and Mika 2009; Mateus et al. 2009; Puysségur, Michel, and Avouac 2007). Some cases demonstrate that the NWP model may underestimate the spatial variation in the delay (Liu, Hanssen, and Mika 2009), due to initial condition errors (which can be partially mitigated by data assimilation) and/or model errors (such as from sub-grid-scale physical parameterization schemes). Also, SAR data have a spatial resolution that is sometimes two orders of magnitude greater than that of NWP (e.g. about 30 m for Envisat ASAR data *versus* >1 km for most NWP simulations). To obtain more realistic and accurate predictions of atmospheric water vapour content, therefore, further research is needed to explore the use of more accurate NWP models with finer resolution as well as improved initial conditions. The operational NWP centres around the world obtain the initial conditions for their forecast models through ‘data assimilation’, a statistical combination of observations and short-range forecasts (Kalnay 2003). So it is of great significance to use data assimilation to combine various observational data with the NWP model to better simulate the water vapour.

This study provides an inter-comparison of three methods – high-resolution convection-permitting WRF model simulations (both with and without additional mesoscale data assimilation), and coarse-resolution global meteorological analysis data – used to estimate the tropospheric water vapour content during the two SAR overpasses. Key questions to be addressed include: (1) How much does atmospheric water vapour affect the InSAR measurements of the surface deformation? (2) How accurate are atmospheric water vapour estimations by convection-permitting NWP simulations? (3) Will additional mesoscale data assimilation for the high-resolution NWP simulations further improve the accuracy of estimated atmospheric water vapour content?

2. Atmospheric phase delay in InSAR

The phase observed by InSAR can be decomposed into a linear combination of the following phase contributions:

$$\varphi_{\mathrm{InSAR}} = \varphi_{\mathrm{orbit}} + \varphi_{\mathrm{topography}} + \varphi_{\mathrm{noise}} + \varphi_{\mathrm{deformation}} + \varphi_{\mathrm{atmosphere}}, \quad (1)$$

where φ_{InSAR} is the differential interferometric phase between two acquisition times, φ_{orbit} is the phase due to the 'curved Earth' geometry (which can be removed by a precise InSAR orbit), $\varphi_{\mathrm{topography}}$ is the topographic phase that can be removed by subtracting a simulated topographic phase from a digital elevation model (DEM), and φ_{noise} is phase noise (due to the decorrelation of the InSAR signal by vegetation or change of the surface environment). We are concerned with the last two terms on the right-hand side of Equation (1): $\varphi_{\mathrm{deformation}}$, the phase by surface movement along the radar line of sight (LOS) direction, and $\varphi_{\mathrm{atmosphere}}$, the phase contributed by atmosphere, particularly the difference in atmospheric signal contributions between the two passes. In this article, our main goal is to separate $\varphi_{\mathrm{atmosphere}}$ from $\varphi_{\mathrm{deformation}}$ using different methods. In order to obtain $\varphi_{\mathrm{atmosphere}}$, we will look into the factors that affect radar wave propagation. When a radar wave propagates through the atmosphere, it will be delayed and bent due to the differential refraction within the spatially heterogeneous atmosphere. Here we can ignore the extra length due to bending because we are interested in the difference between the two curved paths illuminated by a radar sensor at different observation times (Zebker, Rosen, and Hensley 1997). Some studies also indicate that the bending error can be ignored for zenith angles of less than 87° (Bean and Dutton 1968). Therefore, we only take the propagation delay into account. The zenith atmospheric delay, $\Delta L_{\mathrm{atmosphere}}$ between two acquisition times can be expressed as (Hanssen 2001)

$$\Delta L_{\mathrm{atmosphere}} = \Delta L_{\mathrm{ZHD}} + \Delta L_{\mathrm{ZWD}} + \Delta L_{\mathrm{ionosphere}} + \Delta L_{\mathrm{liquid}}, \quad (2)$$

where ΔL_{ZHD} is the zenith hydrostatic delay (ZHD), ΔL_{ZWD} is the zenith wet delay (ZWD) due to water vapour, $\Delta L_{\mathrm{ionosphere}}$ is the zenith ionospheric delay, and $\Delta L_{\mathrm{liquid}}$ is the zenith liquid delay caused by liquid water. Both $\Delta L_{\mathrm{ionosphere}}$ and $\Delta L_{\mathrm{liquid}}$ can be ignored for the C-band frequency because these have a minimal impact on InSAR observations (Hanssen 2001). Although ΔL_{ZHD} is mainly affected by dry air processes, it does include a contribution from water vapour (due to the non-dipole component of water vapour refractivity (Bevis et al. 1992)). The magnitude of L_{ZHD} is much larger than that of L_{ZWD}, but the latter is usually far more variable: in temperate areas, the daily variability in ΔL_{ZWD} usually exceeds that of ΔL_{ZHD} by an order of magnitude (Bevis et al. 1996). This is because L_{ZHD} is proportional to surface pressure, a quantity that typically fluctuates by 0.1–0.2% over a day and rarely by more than 0.5%; however, L_{ZWD} is nearly proportional to the integrated water vapour (IWV), which can easily fluctuate by 50–100%. Because ΔL_{ZHD} has minimal spatial and temporal variation, it can be eliminated during the interferogram differential step and thus can be ignored in our study, which is mainly focused on the impact of water vapour. Estimates of

ΔL_{ZWD} can be derived from IWV or precipitable water vapour (PWV) of two SAR acquisitions using a conversion factor Π (which is dependent on the surface temperature):

$$\begin{aligned}\Delta L_{\mathrm{ZHD}} &= \Pi \times \Delta(\mathrm{IWV}) = \Pi \times \rho_{\mathrm{water}} \times \Delta(\mathrm{PWV}) \\ &= \Pi \times \rho_{\mathrm{water}} \times \left((\mathrm{PWV})_{\mathrm{date1}} - (\mathrm{PWV})_{\mathrm{date2}}\right),\end{aligned} \tag{3}$$

where Δ(IWV) and Δ(PWV) are the differences of IWV and PWV, respectively, between two acquisition times, and $(\mathrm{PWV})_{\mathrm{date1}}$ and $(\mathrm{PWV})_{\mathrm{date2}}$ are the PWV of two SAR acquisition dates. Conversion factor Π can be calculated from surface temperature observations with a relative root mean square error (RMSE) of about 2% (Bevis et al. 1992), and shows little variability in a SAR frame. The value of Π ranges from 6.0 to 6.5 and is often approximately 6.2 (Bevis et al. 1992; Li, Muller, and Cross 2003; Li et al. 2005; Niell 2001). Because the radar incidence angle $\theta_{\mathrm{incidence}}$ is small (about 23° of Envisat ASAR data), ΔL_{ZWD} can be mapped to the radar's LOS direction by a $\cos\theta_{\mathrm{incidence}}$ function, rather than tracing the ray paths through the three-dimensional (3D) water vapour field (Foster et al. 2006; Hobiger et al. 2010). In this study, IWV and PWV can be obtained from WRF model output and Final Operational Global Analysis (FNL) data. The slant phase delay, $\Delta\varphi_{\mathrm{atmosphere}}$ induced by the presence of atmospheric water vapour can be calculated via

$$\Delta\,\varphi_{\mathrm{atmosphere}} = \frac{4\pi\,\Delta\,L_{\mathrm{ZWD}}}{\lambda\cos\theta_{\mathrm{incidence}}}, \tag{4}$$

where λ is the radar wavelength. Then $\Delta\varphi_{\mathrm{atmosphere}}$ is subtracted from the original interferogram to obtain the atmospheric-corrected interferogram. The corrected interferogram is used with InSAR processing to obtain the baseline-refined atmospheric-corrected interferogram. We use this atmospheric-corrected interferogram to obtain the deformation map of the study site by the following equation, which shows that the phase shift is directly proportional to path length:

$$L_{\mathrm{deformation}} = \frac{\lambda\varphi_{\mathrm{deformation}}}{4\pi}, \tag{5}$$

where $\varphi_{\mathrm{deformation}}$ is the unwrapped atmospheric-corrected interferogram and $L_{\mathrm{deformation}}$ is the deformation in radar LOS deformation.

3. Methodology

3.1. Water vapour derived from various numerical model analyses and simulations

In this study, we propose three different ways to estimate atmospheric water vapour (described below), which are then used to correct for the atmospheric effects in the InSAR measurements of surface deformation.

3.1.1. NCEP GFS-FNL

The first method used for atmospheric correction of the InSAR measurements is the archived National Centers for Environmental Prediction (NCEP)'s FNL based on NCEP's Global Forecast System (GFS, a global NWP model). This GFS-FNL data set has a spatial resolution of 1° × 1° (about 80 km × 80 km for the study region), available every 6 hours and produced by the Global Data Assimilation System through assimilating observations from the Global Telecommunications System (GTS) and other sources. The meteorological variables in GFS-FNL include, but are not limited to, air temperature, cloud top pressure, humidity, surface winds, upper-level winds, and precipitable water, the last of which is used for atmospheric correction.

For each acquisition date, the PWV values estimated by GFS-FNL at 0000 UTC and 0600 UTC are linearly interpolated to 0230 UTC, which is the SAR acquisition time. Differential PWV maps are produced using the temporally interpolated data from the two SAR acquisition dates. These differential water vapour maps are then interpolated in space (using a cubic convolution) to the same resolution as the InSAR data. From these spatially interpolated differential water vapour maps, the differential water vapour delay in phase can be calculated using Equations (3) and (4).

3.1.2. WRF simulation initialized with FNL (WRF-FNL) without additional mesoscale data assimilation

The Advanced Research WRF (WRF-ARW) is a state-of-the-art, limited-area NWP system widely used for research and operations from meso- to convective scales (Skamarock et al. 2008). The model used here is version 3.5 of WRF-ARW, available since April 2013. The WRF model is fully compressible and nonhydrostatic, with a large number of parameterization schemes for sub-grid-scale processes including cumulus convection, cloud microphysics, radiation, and land-surface processes. It has a terrain-following vertical coordinate and multiple nesting capabilities. Output data from the WRF model can be used to generate the 3D water vapour field at a given time, from which the wet components of atmospheric delay can be calculated.

To enhance the WRF model resolution over the SAR image area, three two-way nested domains inside a parent outer domain are used (Figure 1(*a*)). The parent domain (D01) has a horizontal grid spacing of 27 km and covers most of South China. The two solid boxes in Figure 1(*a*) (D02 and D03) correspond to nested domains with 9 and 3 km horizontal grid spacing, respectively. The dashed box in Figure 1(*a*) shows the location of D04, which has a horizontal grid spacing of 1 km and greatly overlaps the SAR data

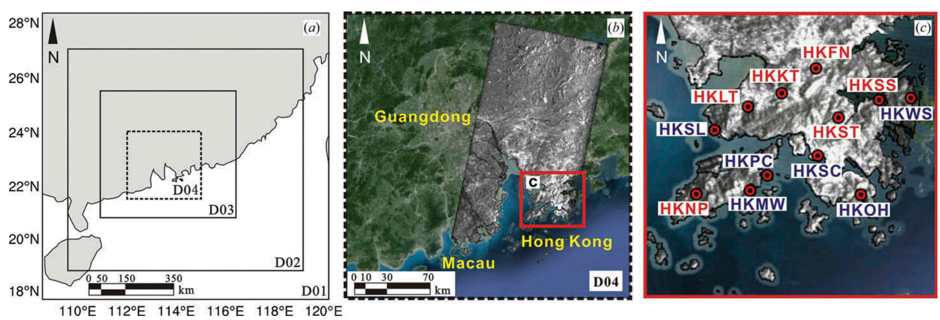

Figure 1. (*a*) Configuration of WRF domains. (*b*) SAR intensity image in D04; red box denotes the domain of (*c*). (*c*) Locations of permanent ground-based GPS stations (names in blue and red) in Hong Kong. All 12 GPS stations are used in the PWV verification; six stations (labelled in red) that overlapped with the SAR interferogram are employed to validate the deformation.

swath (Figure 1(*b*)). Twenty-seven vertical levels are used in each simulation, and the model's initial and lateral boundary conditions are generated from GFS-FNL data. For both WRF model start dates – 3 January and 14 March 2009 – the start time is set to 1200 UTC, about 14 hours before SAR acquisitions. In D01 and D02, convection is parameterized using the Kain–Fritsch cumulus scheme (Kain 2004); in the innermost domains (D03 and D04), convection is resolved explicitly – that is, these domains (with horizontal grid spacings of 3 and 1 km, respectively) can be regarded as 'convection-permitting'. In all domains, atmospheric water vapour, as well as liquid water and ice, is handled by the WRF Single Moment 3-class (WSM3) microphysics scheme (Hong, Dudhia, and Chen 2004). Because there is no substantial reported precipitation from moist processes in the study domain during either simulation period, selection of the microphysics and cumulus schemes will not directly affect the atmospheric corrections in this case study. The parameters in the WRF output files, including water vapour mixing ratio, pressure, and temperature, are used to calculate the water vapour content in each layer and finally to obtain the IWV. Two WRF simulations (both configured as described above) are run in this study. The first, hereafter referred to as WRF-FNL, derives its initial conditions directly from the GFS-FNL data. The second simulation – WRF-DA, discussed below – uses data assimilation to improve upon the GFS-FNL-derived initial conditions.

3.1.3. WRF simulation initialized with additional mesoscale data assimilation (WRF-DA)

The WRF data assimilation system (Huang et al. 2009) includes a 3D variational data assimilation algorithm (3DVar, Barker et al. 2004). Data assimilation is the technique by which observations are combined with the first guess (the background) from a NWP model and relevant error statistics in an optimal way to provide an improved estimate (the analysis) of the atmospheric state (Talagrand 1997). Variational data assimilation achieves this through the iterative minimization of a prescribed cost function. Differences between the analysis and the observations/background are penalized depending on their perceived error. The cost function to be minimized in the WRF-3DVar data assimilation system is (Barker et al. 2004; Huang et al. 2009)

$$2J(x) = (x - x_\mathrm{b})^\mathrm{T}\,\mathbf{B}^{-1}(x - x_\mathrm{b}) + (y_\mathrm{o} - H(x))^\mathrm{T}\,\mathbf{R}^{-1}(y_\mathrm{o} - H(x)), \tag{6}$$

where x_b is the background field, $\mathbf{B}$ is the background error covariance matrix, y_o is the observations, and $\mathbf{R}$ is the observation error covariance matrix; these elements are all inputs from users. $J(x)$ is the scalar cost function, x is the analysis, and $H(x)$ is the observation operator; these three elements are the outputs from the WRF 3DVar data assimilation system.

For the WRF-DA experiment in this study, we use the observations from GTS, which include, but are not limited to, wind speed and direction, pressure, geopotential height, air temperature, dew point, and precipitation amount. These observations are mainly from surface observations, synoptic radiosondes, aircraft reports, GPS refractivity measurements, and data from satellites (such as the SeaWinds instrument on QuikSCAT). The observations are from NCEP ADP global surface and upper air observational weather data (NCEP 2008). The number of observations in D01 within 1 hour of the model start time (1200 UTC) is 562 on 3 January 2009 and 314 on 14 March 2009; these observations are mainly located near Hong Kong. Specifically, the

562 observations on 3 January 2009 comprise 328 from QuikSCAT (SeaWinds), 134 aircraft reports (Airep), and 55 surface synoptic observations (Synop); the remaining 45 reports are from radiosondes, Meteorological Terminal Aviation Routine Weather Report (METAR), upper-wind reports (Pilot), and ships. The 314 observations on 14 March 2009 comprise 211 Airep and 55 Synop, with the remaining 48 from radiosondes, METAR, Pilot, and ships. These observations are from GTS, which are part of the assimilated observations in the GFS (note that FNL is the operational analysis of the GFS). Only operational observations – those that are available in near real time – are assimilated into FNL (Carvalho et al. 2014). Although the observations in WRF-DA may have already been included in the FNL analysis, it is common practice in regional-scale modelling to perform additional data assimilation using the global analysis as a background to generate initial conditions for high-resolution mesoscale models (Ahasan and Debsarma 2015). After assimilating the observations mentioned above to derive the initial conditions, we run the WRF model to produce updated outputs and then obtain the water vapour content.

It is worth noting that although 3DVar is not the most advanced data assimilation system available in WRF (Meng and Zhang 2008; Zhang, Zhang, and Poterjoy 2013), it is the most computationally affordable and the easiest to implement. Nevertheless, future research will examine the impact of using more advanced data assimilation methods such as the ensemble Kalman filter, four-dimensional variational data assimilation, and their hybrids (Zhang and Zhang 2012; Zhang, Zhang, and Poterjoy 2013) in the atmospheric correction of InSAR measurements.

3.2. InSAR data and processing

The InSAR data used in this study are from Envisat ASAR operated by the European Space Agency and obtained around 0230 UTC on both 4 January and 15 March 2009, and the perpendicular baseline is 365 m. The study site (Figure 1(*b*)) is located in the Pearl River Delta region, China. It includes parts of Guangdong Province, Hong Kong, and Macau. Figure 1(*b*) shows the geocoded SAR intensity image generated from Envisat ASAR data that were processed using the repeat-orbit interferometry package (ROI_PAC) software, developed at the Jet Propulsion Laboratory and California Institute of Technology (Rosen et al. 2004). The InSAR processing can be divided into several main steps: SAR image formation, co-registration, interferogram formation, flattening (using precise orbits from ESA), topography removing (using a three arc-second (about 90 m) DEM from the Shuttle Radar Topography Mission), unwrapping (using Statistical-cost, Network-flow Algorithm for Phase Unwrapping (SNAPHU) (Chen and Zebker 2002)), baseline re-estimation, and finally geocoding. The above InSAR processing was further adjusted to include atmospheric correction. Because the atmospheric signal introduces a phase artefact similar to that of the residual orbit phase, several studies have suggested applying water vapour corrections to the unwrapped phase first and then using the corrected unwrapped phase to refine the baseline (Buckley et al. 2003; Li, Fielding, et al. 2006). For this study, the differential water vapour is first converted to the phase delay in the LOS via Equation (4). Second, the phase is mapped from the geographic coordinate system to the radar coordinate system. Third, this atmospheric phase is subtracted from the original unwrapping interferogram generated after the unwrapping step. Last, this unwrapped interferogram after water vapour correction comes to the baseline refinement and is then geocoded.

3.3. GPS verification

GPS data are used in this study as verification for two purposes: the first for comparison of the PWV from meteorological methods in order to evaluate the model simulation accuracy, the second to validate the surface deformation derived from InSAR. Ground-based GPS has become an operational tool that can measure PWV with high accuracy (1.0–1.5 mm) and high temporal resolution (5 s in this study) (Li 2004). Here, we verify PWV estimates from the NCEP GFS-FNL interpolation and WRF-FNL and WRF-DA simulations against the GPS observations from the 12 ground-based stations as part of the Hong Kong Satellite Positioning Reference Station Network (Figure 1(*c*)). These GPS data are not assimilated in the WRF-DA experiment. Six of these stations overlapping with the SAR interferogram are used to validate the atmospheric correction results over the Hong Kong area. The GPS data are collected over a continuous 24-hour period. We deduce PWV from the GPS observations using version 10.4 of GAMIT/GLOBK (a high-accuracy GPS processing software package). After post-processing of precise point positioning by GAMIT/GLOBK software, we can obtain the latitude, longitude, and ellipsoidal height of each GPS station accurate to the millimetre level. We use the ellipsoidal height of the two dates to produce the differential displacements of height and then map these GPS-derived height offsets into the radar LOS direction by $\cos\theta_{\mathrm{incidence}}$ (Foster et al. 2006).

4. Results and discussion

4.1. Phase of atmospheric signals

Here we analyse the differential phase of water vapour derived by different methods. Figure 2(*a*) shows the initial DInSAR unwrapped phase without atmospheric correction. Note that the ocean (white) has been masked during DInSAR processing. Relatively high magnitudes of differential phase are located in the western and northwestern parts of the domain, as well as in Hong Kong. Figures 2(*b*)–(*d*) show the phase of the atmospheric signal ($\Delta\varphi_{\mathrm{atmosphere}}$) derived from the water vapour estimated by the GFS-FNL, WRF-FNL, and WRF-DA experiments, respectively. It is obvious that the atmospheric signal from the coarse-resolution (1° × 1°) NCEP GFS-FNL data can only capture the large-scale variations in water vapour distribution (with generally higher phase difference in the

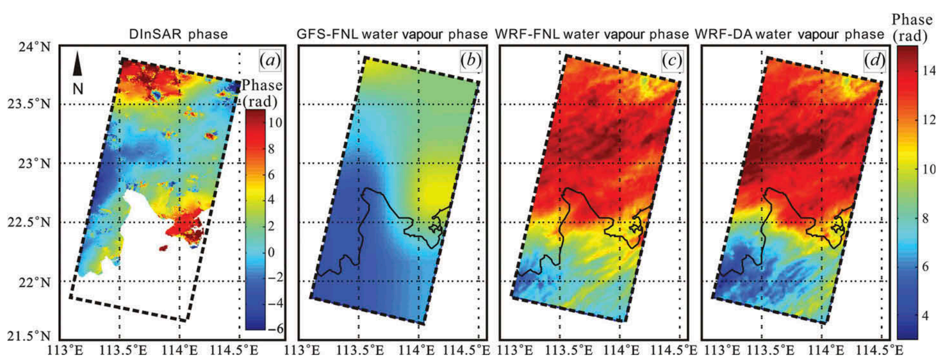

Figure 2. (*a*) Original DInSAR unwrapped phase. (*b*)–(*d*) Water vapour phases in LOS direction from NCEP GFS-FNL data, WRF-FNL, and WRF-DA, respectively. The black line in (*b*)–(*d*) marks the coastline.

northern and eastern portions of the domain). In contrast, the phase differences estimated from the water vapour in the 1 km domains (D04) of both high-resolution WRF simulations (WRF-FNL and WRF-DA, Figures 2(*c*) and (*d*)) exhibit much finer (small-scale) variability and have considerably higher phase difference values over land (northern two-thirds of the domain) than over the sea and coastal areas. Water vapour phase estimates from the two high-resolution WRF simulations share similar spatial patterns, except over the southwest portion of the domain (where the IWV in WRF-DA is higher than that in WRF-FNL) and (to a lesser extent) in areas near the coastline. Moreover, the overall phase difference estimated with the GFS-FNL interpolated analysis is much smaller than the phase differences estimated from WRF-FNL and WRF-DA, especially over both coastal areas and land. The magnitude of and spatial differences in estimated atmospheric phase delay are derived exclusively from the differences in estimated atmospheric water vapour estimation from the various NWP model products (to be discussed in detail in Section 4.3).

4.2. *Atmospheric effect mitigation*

Figures 3(*b*)–(*d*) show the deformation maps after atmospheric correction by different NWP model products. For the sake of comparison, the deformation map from the initial unwrapped interferogram is made using Equation (5) and is shown in Figure 3(*a*). After atmospheric correction using the NCEP GFS-FNL water vapour results (Figure 3(*b*)), the deformation magnitude is generally larger than the uncorrected one, although the overall spatial pattern remains nearly identical. However, after atmospheric correction based on WRF-FNL (Figure 3(*c*)) and WRF-DA (Figure 3(*d*)), it is clear that the positive signals in the northwest and Hong Kong and the negative signal in the west have been largely removed: the range of the middle 95% distribution (that is, excluding the lowest 2.5% and highest 2.5%) of deformation values decreases from −20 mm, +43 mm to −13 mm, +26.5 mm, which renders the corrected interferogram much flatter. A relatively high (corrected) deformation value of about 35 mm is measured in the northwest corners of both WRF-FNL and WRF-DA. This corresponds to a forested area with low coherence, where the quality of the InSAR interferogram is poor. The deformation maps derived from the WRF-FNL and WRF-DA simulations (Figures 3(*c*) and (*d*)) exhibit very

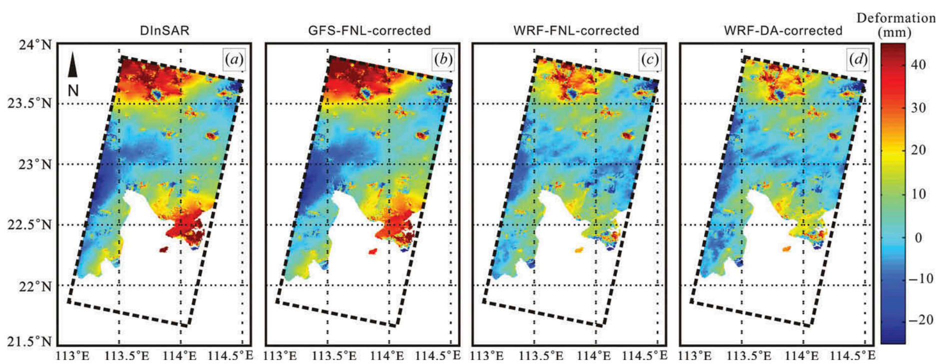

Figure 3. (*a*) Deformation map in the radar LOS direction before atmospheric correction. (*b*) As in (*a*), but after atmospheric correction using NCEP GFS-FNL water vapour data. (*c*) As in (*b*), but using WRF-FNL. (*d*) As in (*b*), but using WRF-DA.

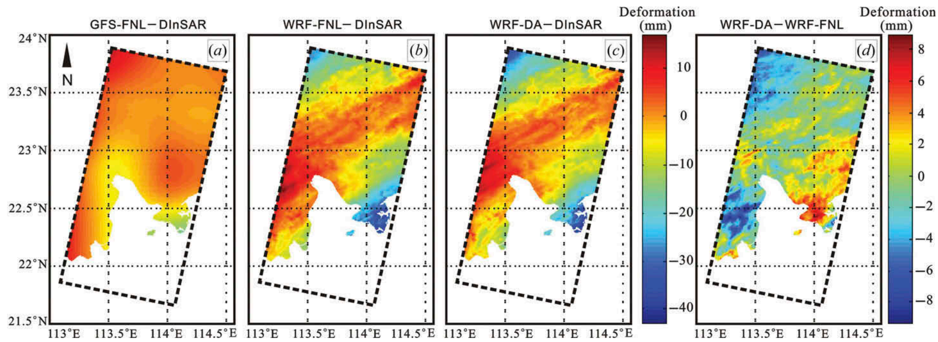

Figure 4. Deformation differences between the original DInSAR and (*a*) NCEP GFS-FNL data; (*b*) WRF-FNL; and (*c*) WRF-DA. The deformation difference between WRF-DA and WRF-FNL is shown in (*d*).

high-frequency spatial features in the middle of the domain. These features, with horizontal scales of around 10 km or less, are likely a consequence of small-scale variability and uncertainty in atmospheric water vapour from the WRF simulations (Figures 2(*c*) and (*d*)) rather than a reflection of the real spatial variability in surface deformation at such fine scales during the study period.

Figures 4(*a*)–(*c*) show the differences between the atmospheric-corrected surface deformation (Figures 3(*b*)–(*d*)) and the uncorrected values (Figure 3(*a*)). These deformation differences are due solely to the phase differences in accounting for the effects of atmospheric water vapour derived from the three different NWP model products. From these different NWP products, we can see that the atmospheric signal observed in repeat-pass SAR in this study can lead to deformation differences between about −43 and +17 mm. One striking result is that the deformation differences for GFS-FNL (Figure 4(*a*)) are poorly correlated with the WRF-derived deformation differences (Figures 4(*b*) and (*c*)): in the northwest corner of the domain and around (22.75° N, 114° E), there are large positive (negative) deformation differences in the GFS-FNL (WRF-derived) results. Although it is very difficult to verify, this result suggests (and is supported by Figure 5) that the coarser resolution of the GFS-FNL does not accurately represent important smaller-scale atmospheric processes (captured by WRF) that determine the water vapour distribution in this region. The WRF-DA and WRF-FNL deformation maps are very similar (Figure 4(*d*)), except along the coast where the deformation differences are in the order of ±8 mm.

4.3. Inter-comparison of IWV

Comparison of IWV derived from NCEP GFS-FNL data, WRF-FNL, and WRF-DA is shown in Figure 5. It is apparent that the water vapour level was higher on 4 January 2009 than on 15 March 2009, resulting in a significant atmospheric phase delay in DInSAR. Therefore it is necessary to estimate and eliminate such atmospheric effects. As stated above and evident from Figure 5, NCEP GFS-FNL data cannot resolve key small-scale features of water vapour distribution: the GFS-FNL result (Figures 5(*a*) and (*b*)) for both days has a strong WNW–ESE gradient while the WRF results have a N–S gradient, so it is not ideal to use such coarse-resolution NWP analysis data directly to estimate atmospheric delay. The third column in Figure 5 is the differential IWV between

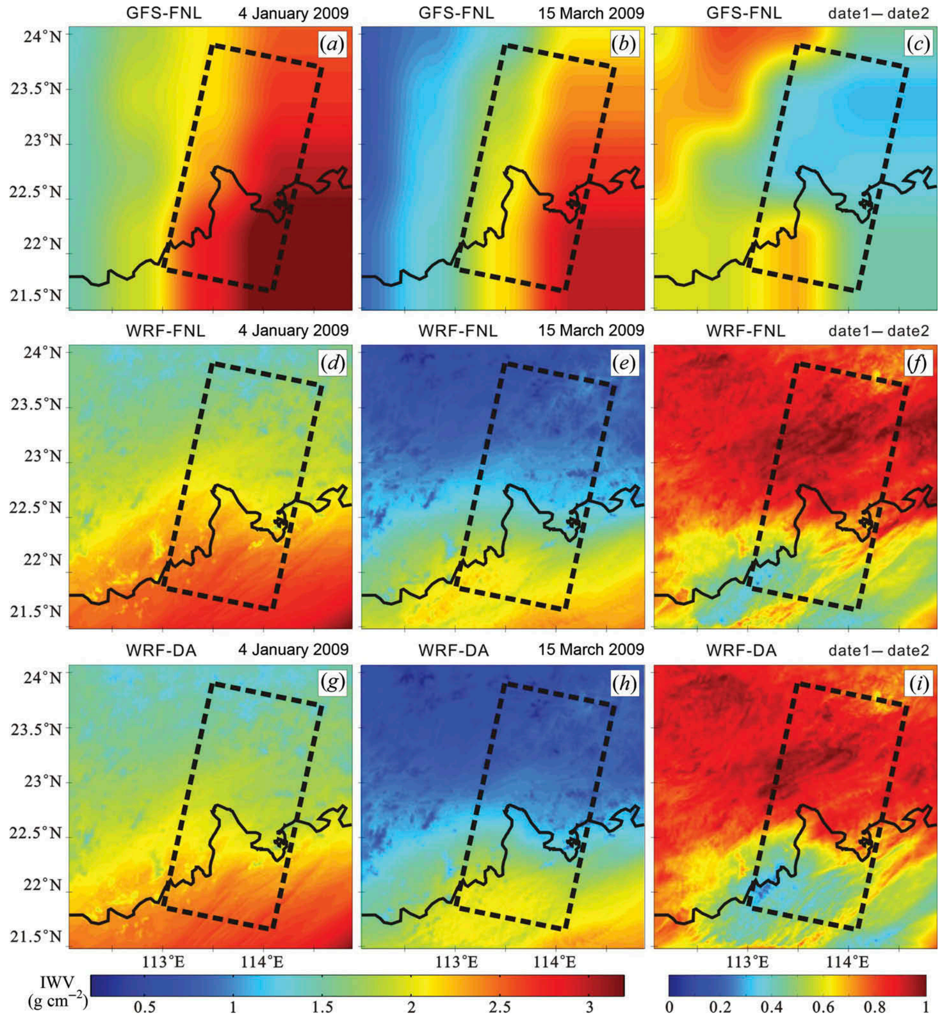

Figure 5. Integrated water vapour (IWV) (corresponding to D04 in Figure 1(*a*)) derived from (*a*)–(*c*) interpolated NCEP GFS-FNL data, (*d*)–(*f*) WRF-FNL, and (*g*)–(*i*) WRF-DA. (*a*), (*d*), (*g*) are valid on 4 January 2009 and (*b*), (*e*), (*h*) are valid on 15 March 2009. (*c*), (*f*), (*i*) are the differences in IWV between 4 January (date 1) and 15 March (date 2). The dashed rectangles indicate the domain of the InSAR data (cf. Figure 1(*b*)).

the two dates (4 January minus 15 March). From Figures 5(*f*) –(*i*), it can be seen that the discrepancies between WRF-FNL and WRF-DA are mainly along the coastline where more observations were gathered, consistent with the rather small difference in corrected surface deformation between these two methods (Figures 3(*c*) and (*d*)).

Figure 6 also shows the differences in IWV between WRF-FNL and WRF-DA at the two InSAR pass times, and the differential result between the differences of the two dates. On 4 January (Figure 6(*a*)), the IWV from WRF-DA is lower than that of WRF-FNL near the Pearl River Delta. Also, the IWV difference between WRF-DA and WRF-FNL is greater on 4 January (Figure 6(*a*)) than on 15 March (Figure 6(*b*)). It should be mentioned that the IWV on 4 January is greater than on 15 March, which indicates that the former is

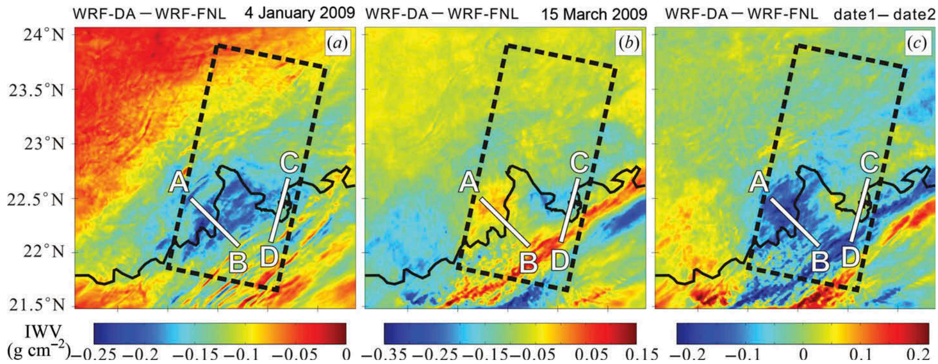

Figure 6. IWV from WRF-DA minus IWV from WRF-FNL for (*a*) 4 January 2009 (the same as Figure 5(*g*) minus 5(*d*)) and (*b*) 15 March 2009 (the same as Figure 5(*h*) minus 5(*e*)). (*c*) Differential result between the two dates, which is (*a*) minus (*b*) (the same as Figure 5(*i*) minus 5(*f*)). The white lines indicate the cross-sections in Figures 7 and 8.

moister than the latter. So in the moister environment, the difference between WRF-DA and WRF-FNL is higher than in the drier environment. Combining the results of these two dates, we obtain the discrepancy of the differential IWV (Figure 6(*c*)). It is clear that the difference in Figure 6(*c*) is along the coastline area, with a magnitude of about 0.2 g cm^{-2}. This difference leads to a deformation of about 8 mm after atmospheric correction and InSAR baseline refinement (see Figure 4(*d*) for comparison). Meanwhile, the coastline areas with a significant land–sea difference had more observations than the other parts of study site. The differences along the coastline indicate that additional mesoscale data assimilation of coastal observations had a substantial impact on the high-resolution WRF simulations. Therefore, it may be advantageous to incorporate further observations via mesoscale data assimilation to improve the performance of NWP simulations for the purpose of mitigating atmospheric effects in InSAR measurements.

4.4. Vertical profile of water vapour

We chose two cross-sections – denoted AB and CD – near the coastline (see Figure 6 for location), to compare the vertical distribution of water vapour between WRF-FNL and WRF-DA. The differences along cross-sections AB and CD are shown in Figures 7 and 8, respectively, from the surface to a height of 6 km. Not surprisingly, the greatest concentrations of water vapour are near the surface, with nearly negligible moisture at 6 km (Figures 7(*a*), (*b*), (*d*), (*e*) and 8(*a*), (*b*), (*d*), (*e*)). The horizontal gradients in water vapour – with more moisture over water (right-hand side of cross-sections) than over land (left-hand side of cross-sections) – are generally confined to the lowest 2 km of the atmosphere. Therefore, for the purposes of atmospheric correction, it is essential to capture accurately the atmospheric processes associated with air–sea–land interactions (such as sea breezes, coastal fronts, surface fluxes, and turbulent boundary layer fluxes). As mentioned above, additional mesoscale data assimilation of finer-scale observations, especially those near the ground, may further improve estimates of atmospheric water vapour (cf. Figures 7(*g*), (*h*) and 8(*g*), (*h*)), although future studies or field campaigns are needed to verify the fidelity of the finer-scale estimation of water vapour content by high-resolution, convection-permitting NWP model simulations.

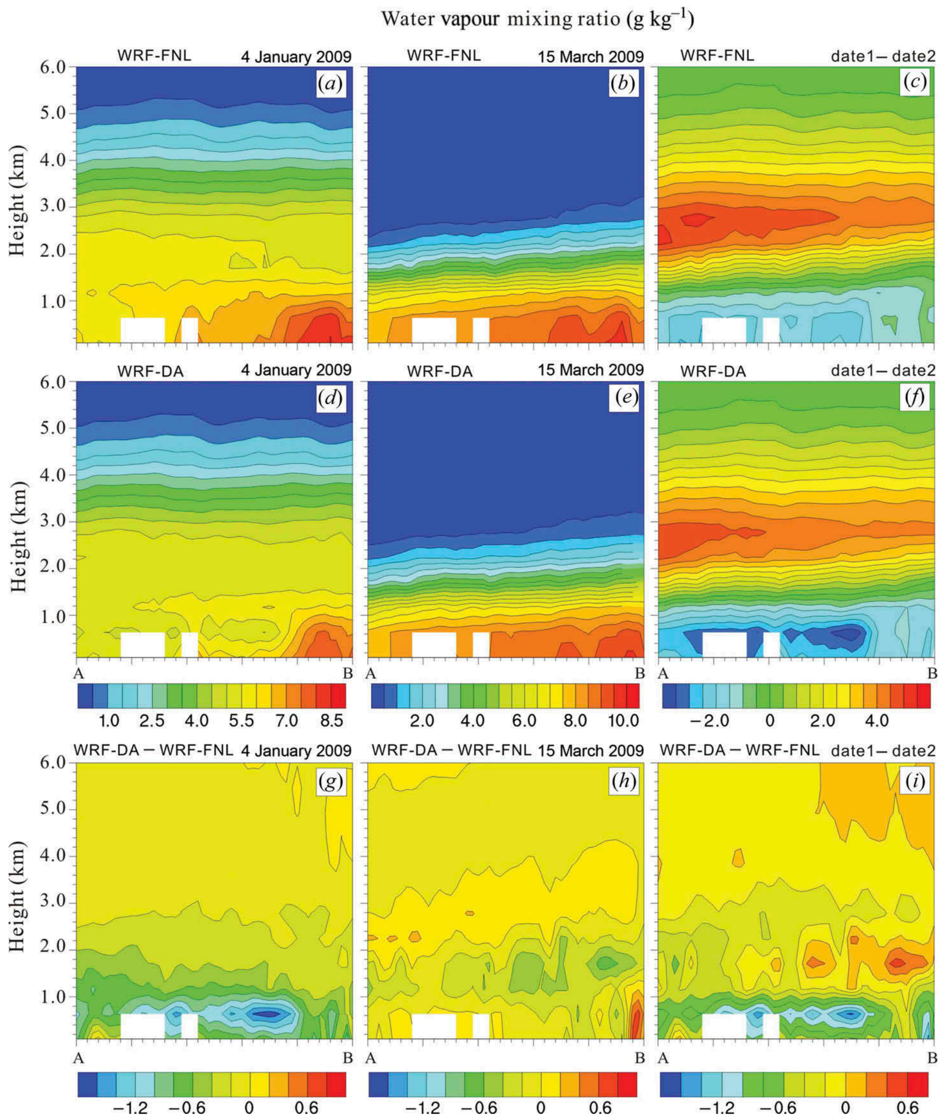

Figure 7. Vertical profiles of water vapour mixing ratio along cross-section AB (Figure 6) from (*a*)–(*c*) WRF-FNL and (*d*)–(*f*) WRF-DA. (*a*), (*d*) are valid on 4 January 2009 and (*b*), (*e*) are valid on 15 March 2009. (*c*), (*f*) are the water vapour mixing ratios on 4 January (date 1) minus those on 15 March (date 2). (*g*)–(*i*) are the differences between (*a*)–(*c*) and (*d*)–(*f*), respectively.

4.5. Verification by GPS data

Figure 9 shows the PWV from NCEP GFS-FNL data and WRF-FNL, WRF-DA, and GPS (observations) at the two SAR acquisition times (0230 UTC on 4 January and 15 March 2009) at the locations of the GPS sites. Clearly, the bias in PWV from NCEP GFS-FNL data is substantially higher than those from WRF-FNL and WRF-DA. The larger bias in the NCEP GFS-FNL PWV is most likely the result of the coarser horizontal resolution (1° × 1° grids), which can induce a representative error – especially over coastal areas where PWV is quite variable. The RMSE for each of the three model data sets (using GPS data as the truth)

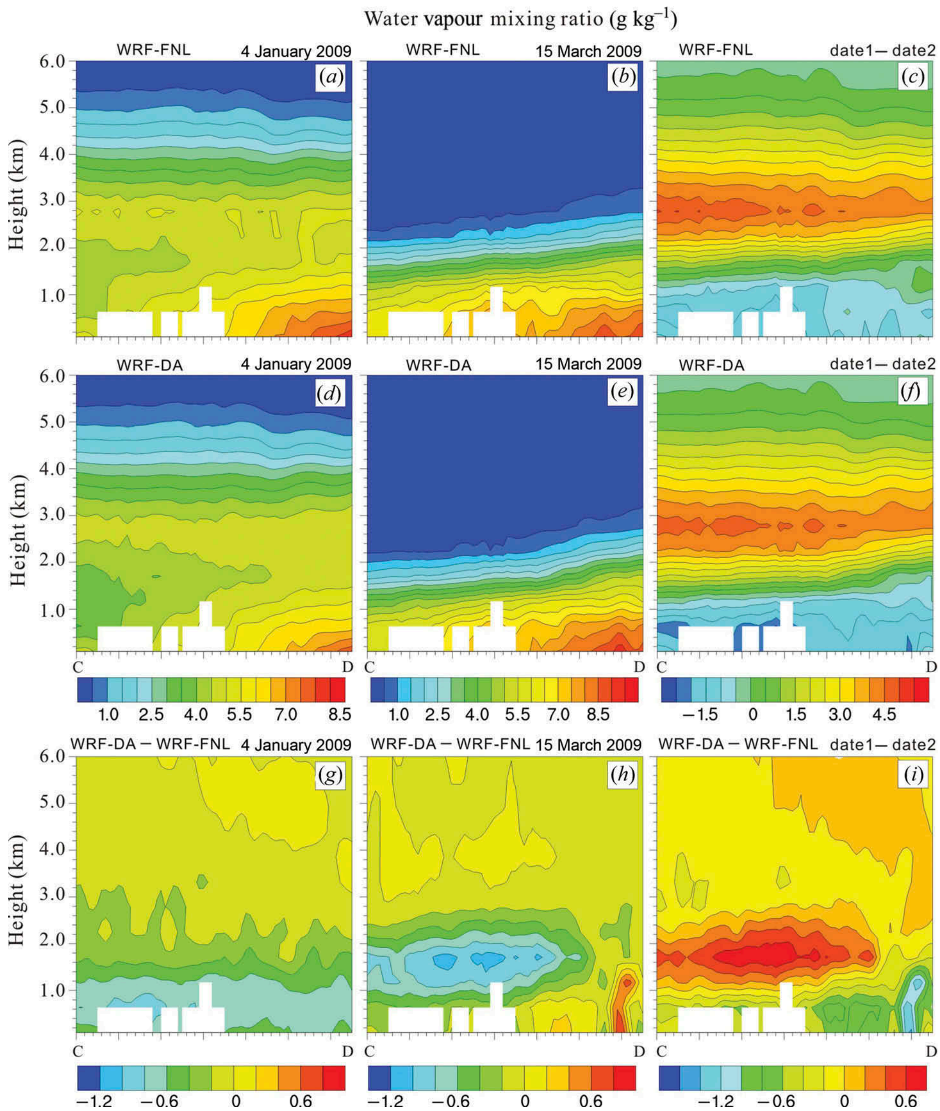

Figure 8. As in Figure 7, but for cross-section CD (see Figure 6).

is also shown in Figure 9. By this metric, the most accurate PWV field is derived from WRF-DA, with differences of generally less than 3 mm. It is important to reiterate that the GPS data were not assimilated into WRF-DA, and thus are a fully independent validation of PWV.

Six of the 12 GPS stations are used in the deformation verification (see Figure 1(*c*)). Comparisons of range changes derived from InSAR and GPS techniques are performed by mapping the GPS-derived displacements, which is the relative offset of two dates, into the radar LOS direction (Figure 10). Figure 10 shows that applying atmospheric correction decreases the relatively large displacement (of the uncorrected InSAR measurements) by up to 30 mm, yielding values that are closer to those of GPS. Not surprisingly, applying atmospheric correction with NCEP GFS-FNL data shows a slight reduction (of about

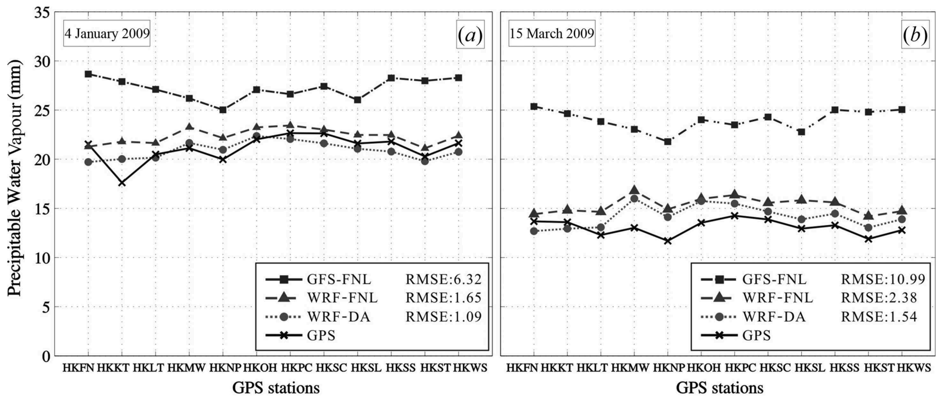

Figure 9. Comparison of precipitable water vapour (PWV) derived by different methods at the locations of the GPS sites at 0230 UTC on (*a*) 4 January 2009 and (*b*) 15 March 2009. Black solid line with cross represents the PWV from GPS, which can be treated as the truth of observations. The dashed dot line with the square is the PWV from NCEP GFS-FNL data at same points with GPS sites. The dashed line with triangle is the PWV from WRF-FNL. The dotted line with round circle is the PWV from WRF-DA. The root mean square error (RMSE) of the three methods *versus* GPS is shown in the legend. The horizontal axis is the name of the GPS site.

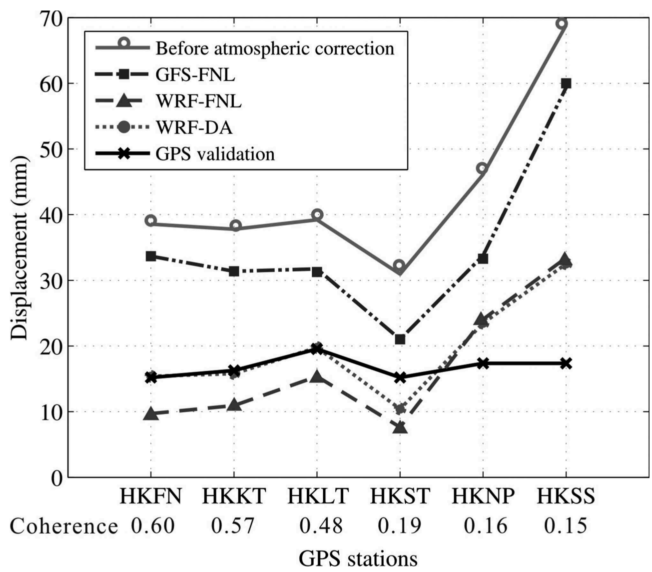

Figure 10. Relative displacement between GPS stations (sorted by coherence) in Hong Kong between 4 January and 15 March 2009 in the radar LOS direction. Black solid line with cross represents the displacement from GPS. Grey solid line with blank circle is the relative LOS displacement from the uncorrected interferogram at same points with GPS. The dashed dotted line with square, triangle, and round circle denotes the relative LOS displacements from the interferogram with the atmospheric correction with NCEP GFS-FNL data, WRF-FNL, and WRF-DA, respectively. The coherence for each station is also shown on the abscissa.

5 mm) in the bias of the deformation. The deformations derived from WRF-FNL and WRF-DA are in much better agreement with the GPS validation, especially so for WRF-DA at the HKFN, HKKT, and HKLT stations. To understand this further, we look at the

coherences of all six stations. Coherence has a major influence on the precision of the InSAR results; high coherence values are associated with 'good quality' whereas low coherence values are associated with 'poor quality' – increasing levels of noise and erratic deformation patterns. The coherence of InSAR data at each GPS station is shown in Figure 10. It indicates that the coherence of HKFN, HKKT, and HKLT, the stations where WRF-DA shows excellent agreement with GPS observations, is higher than that of the other three stations (HKST, HKNP, and HKSS). In the current study, the corrected results at stations with low coherence (that is, 'poor quality' of SAR interferogram) are still biased compared with the GPS validation, suggesting that further studies are necessary to improve the quality of InSAR results and, more importantly, to improve the initial conditions through either better observations or more advanced data assimilation methods for the high-resolution NWP model simulations (e.g. Zhang, Zhang, and Poterjoy 2013).

5. Concluding remarks

In this study, we propose the use of three different model-based data sets – NCEP GFS-FNL data, the WRF model without data assimilation (WRF-FNL), and WRF with 3DVar data assimilation (WRF-DA) – to correct for atmospheric effects in DInSAR. The correction by NCEP GFS-FNL data performed poorly due to its coarse resolution. Both WRF-based data sets (WRF-FNL and WRF-DA) performed substantially better due to the higher resolution of the model. Of these three approaches, WRF-DA provides the best atmospheric correction for DInSAR. The differences in water vapour between WRF-FNL and WRF-DA were greatest along the coastline, where the land–sea difference is substantial. Verification with GPS data concluded that deformation obtained from the WRF-DA-corrected interferogram was the most consistent with the observations at stations with a high coherence. At stations with a low coherence (where the InSAR data are of 'poor quality'), however, all the correction methods had a non-negligible bias.

Overall, this work demonstrates the high potential and effectiveness of WRF-based data assimilation to both reduce water vapour signals and correct the atmospheric phases, despite the fact that few observations – only of standard meteorological data – are assimilated. Future research should focus on making further improvements to NWP model estimates of atmospheric water vapour content, which will result in a more accurate correction of the effects of atmospheric water vapour on InSAR measurements. For example, it is likely that not all observations assimilated by the model have the same impact on the estimated water vapour field; therefore, it is important to determine the location (i.e. surface *versus* upper air or coastline *versus* inland), type (i.e. satellite, radiosonde, etc.), and spatio-temporal density of the observations that result in the greatest improvements to water vapour estimation. In addition, a more advanced data assimilation system – such as the ensemble Kalman filter, four-dimensional variational data assimilation, or their hybrids – is expected to yield even more accurate forecasts; these methods have yet to be tested for DInSAR atmospheric correction and thus will be the focus of ongoing research. Finally, the effects of model error can be investigated by looking at different physical parameterization schemes – particularly for cloud microphysics, which determines the atmospheric water vapour field.

Acknowledgements

The InSAR data were provided by the European Space Agency via the ESA-MOST Dragon 3 Cooperation Program (ID: 10665). The GPS data were provided by Hong Kong Satellite Positioning

Reference Station Network. The NCEP GFS-FNL data are available via the NCAR Research Data Archive (NCEP 2000). The simulation computing was performed at the Texas Advanced Computing Center (TACC). The authors sincerely acknowledge and thank Yonghui Weng, Yue Ying, and Yunji Zhang at Pennsylvania State University and Jian Jiao, Xi'ai Cui, and Siting Xiong at Peking University for their help and invaluable contributions. We also sincerely appreciate the kind suggestions and comments from the reviewer and the editor.

Disclosure statement

No potential conflict of interest was reported by the authors.

Funding

This work was supported by the National Natural Science Foundation of China [41171267] and the National Science and Technology Support Programme of China [2012BAH29B03]. The first author is jointly supported by the Chinese Scholarship Council (CSC) and Pennsylvania State University.

References

Ahasan, M. N., and S. K. Debsarma. 2015. "Impact of Data Assimilation in Simulation of Thunderstorm (Squall Line) Event over Bangladesh Using WRF Model, during SAARC-STORM Pilot Field Experiment 2011." *Natural Hazards* 75 (2): 1009–1022. doi:10.1007/s11069-014-1369-z.

Barker, D. M., W. Huang, Y.-R. Guo, A. Bourgeois, and Q. Xiao. 2004. "A Three-Dimensional Variational Data Assimilation System for MM5: Implementation and Initial Results." *Monthly Weather Review* 132 (4): 897–914. doi:10.1175/1520-0493(2004)132<0897:ATVDAS>2.0.CO;2.

Bean, B. R., and E. Dutton. 1968. *Radio Meteorology*. Vol. 435. New York: Dover Publications.

Bevis, M., S. Businger, T. A. Herring, C. Rocken, R. A. Anthes, and R. H. Ware. 1992. "GPS Meteorology: Remote Sensing of Atmospheric Water Vapor Using the Global Positioning System." *Journal of Geophysical Research: Atmospheres* 97 (D14): 15787–15801.

Bevis, M., S. Chiswell, S. Businger, T. A. Herring, and Y. Bock. 1996. "Estimating Wet Delays Using Numerical Weather Analyses and Predictions." *Radio Science* 31 (3): 477–487. doi:10.1029/96RS00008.

Buckley, S. M., P. A. Rosen, S. Hensley, and B. D. Tapley. 2003. "Land Subsidence in Houston, Texas, Measured by Radar Interferometry and Constrained by Extensometers." *Journal of Geophysical Research: Solid Earth* 108 (B11). doi:10.1029/2002JB001848.

Carvalho, D., A. Rocha, M. Gómez-Gesteira, and C. S. Santos. 2014. "Comparison of Reanalyzed, Analyzed, Satellite-Retrieved and NWP Modelled Winds with Buoy Data along the Iberian Peninsula Coast." *Remote Sensing of Environment* 152: 480–492. doi:10.1016/j.rse.2014.07.017.

Chen, C. W., and H. A. Zebker. 2002. "Phase Unwrapping for Large SAR Interferograms: Statistical Segmentation and Generalized Network Models." *IEEE Transactions on Geoscience and Remote Sensing* 40 (8): 1709–1719. doi:10.1109/TGRS.2002.802453.

Cui, X. A., Q. Zeng, C. Liang, J. Jiao, and Q. Tong. 2012. "Research of InSAR Atmospheric Correction Using WRF Model Simulated Result and MERIS Product." In IGARSS 2012 *International Geoscience and Remote Sensing Symposium*, Munich, Germany.

Ferretti, A., C. Prati, and F. Rocca. 2000. "Nonlinear Subsidence Rate Estimation Using Permanent Scatterers in Differential SAR Interferometry." *IEEE Transactions on Geoscience and Remote Sensing* 38 (5): 2202–2212. doi:10.1109/36.868878.

Foster, J., B. Brooks, T. Cherubini, C. Shacat, S. Businger, and C. Werner. 2006. "Mitigating Atmospheric Noise for InSAR Using a High Resolution Weather Model." *Geophysical Research Letters* 33 (16): L16304. doi:10.1029/2006GL026781.

Foster, J., J. Kealy, T. Cherubini, S. Businger, Z. Lu, and M. Murphy. 2013. "The Utility of Atmospheric Analyses for the Mitigation of Artifacts in InSAR." *Journal of Geophysical Research: Solid Earth* 118: 748–758.

Gong, W., F. Meyer, P. Webley, and D. Morton. 2013. “Performance of the High-Resolution Atmospheric Model HRRR-AK for Correcting Geodetic Observations from Spaceborne Radars.” *Journal of Geophysical Research: Atmospheres* 118 (20): 11611–11624.

Hanssen, R. F. 2001. *Radar Interferometry: Data Interpretation and Error Analysis*. Vol. 2. New York: Springer.

Hobiger, T., Y. Kinoshita, S. Shimizu, R. Ichikawa, M. Furuya, T. Kondo, and Y. Koyama. 2010. “On the Importance of Accurately Ray-Traced Troposphere Corrections for Interferometric SAR Data.” *Journal of Geodesy* 84 (9): 537–546. doi:10.1007/s00190-010-0393-3.

Hong, S.-Y., J. Dudhia, and S.-H. Chen. 2004. “A Revised Approach to Ice Microphysical Processes for the Bulk Parameterization of Clouds and Precipitation.” *Monthly Weather Review* 132 (1): 103–120. doi:10.1175/1520-0493(2004)132<0103:ARATIM>2.0.CO;2.

Huang, X.-Y., Q. Xiao, D. M. Barker, X. Zhang, J. Michalakes, W. Huang, T. Henderson, J. Bray, Y. Chen, Z. Ma, J. Dudhia, Y. Guo, X. Zhang, D.-J. Won, H.-C. Lin, and Y.-H. Kuo. 2009. “Four-Dimensional Variational Data Assimilation for WRF: Formulation and Preliminary Results.” *Monthly Weather Review* 137 (1): 299–314. doi:10.1175/2008MWR2577.1.

Kain, J. S. 2004. “The Kain–Fritsch Convective Parameterization: An Update.” *Journal of Applied Meteorology* 43 (1): 170–181. doi:10.1175/1520-0450(2004)043<0170:TKCPAU>2.0.CO;2.

Kalnay, E. 2003. *Atmospheric Modeling, Data Assimilation, and Predictability*. Cambridge: Cambridge University Press.

Li, Z. 2004. “Production of Regional 1 Km X 1 Km Water Vapor Fields through the Integration of GPS and MODIS Data.” In *The 17th International Technical Meeting of the Satellite Division of the Institute of Navigation ION GNSS*, Long Beach, CA.

Li, Z., E. J. Fielding, P. Cross, and J.-P. Muller. 2006. “Interferometric Synthetic Aperture Radar Atmospheric Correction: GPS Topography-Dependent Turbulence Model.” *Journal of Geophysical Research: Solid Earth* 111 (B2). doi:10.1029/2005JB003711.

Li, Z., J. P. Muller, and P. Cross. 2003. “Comparison of Precipitable Water Vapor Derived from Radiosonde, GPS, and Moderate-Resolution Imaging Spectroradiometer Measurements.” *Journal of Geophysical Research: Atmospheres* 108 (D20). doi:10.1029/2003JD003372.

Li, Z., J.-P. Muller, P. Cross, P. Albert, J. Fischer, and R. Bennartz. 2006c. “Assessment of the Potential of MERIS Near-Infrared Water Vapour Products to Correct ASAR Interferometric Measurements.” *International Journal of Remote Sensing* 27 (2): 349–365. doi:10.1080/01431160500307342.

Li, Z., J. P. Muller, P. Cross, and E. J. Fielding. 2005. “Interferometric Synthetic Aperture Radar (InSAR) Atmospheric Correction: GPS, Moderate Resolution Imaging Spectroradiometer (MODIS), and InSAR Integration.” *Journal of Geophysical Research: Solid Earth* 110 (B3). doi:10.1029/2004JB003446.

Liu, S., R. Hanssen, and A. Mika. 2009. “On the Value of High-Resolution Weather Models for Atmospheric Mitigation in SAR Interferometry.” In *IGARSS 2009 International Geoscience and Remote Sensing Symposium*, Cape town, July 12–17.

Mateus, P., G. Nico, R. Tomé, J. Catalão, and P. Miranda 2009. “Approaches to Mitigate Atmosphere Artefacts in SAR Interferograms: GPS Vs. WRF Model.” In *Proceedings of Fringe* 2009 *Workshop*, Frascati, November 30–December 4.

Meng, Z., and F. Zhang. 2008. “Tests of an Ensemble Kalman Filter for Mesoscale and Regional-Scale Data Assimilation. Part III: Comparison with 3DVAR in a Real-Data Case Study.” *Monthly Weather Review* 136: 522–540. doi:10.1175/2007MWR2106.1.

National Centers for Environmental Prediction/National Weather Service/NOAA/U.S. Department of Commerce. 2000. “National Centers for Environmental Prediction, Updated Daily: NCEP FNL Operational Model Global Tropospheric Analyses, Continuing from July 1999.” Research Data Archive at the National Center for Atmospheric Research, Computational and Information Systems Laboratory, Boulder, CO (Updated daily.). Accessed October 17, 2014. http://dx.doi.org/10.5065/D6M043C6

National Centers for Environmental Prediction/National Weather Service/NOAA/U.S. Department of Commerce. 2008. “NCEP ADP Global Upper Air and Surface Weather Observations (PREPBUFR format), May 1997 – Continuing.” Research Data Archive at the National Center for Atmospheric Research, Computational and Information Systems Laboratory (Updated daily.). Accessed January 16, 2015. http://rda.ucar.edu/datasets/ds337.0/

Niell, A. 2001. "Preliminary Evaluation of Atmospheric Mapping Functions Based on Numerical Weather Models." *Physics and Chemistry of the Earth, Part A: Solid Earth and Geodesy* 26 (6–8): 475–480. doi:10.1016/S1464-1895(01)00087-4.

Puysségur, B., R. Michel, and J.-P. Avouac. 2007. "Tropospheric Phase Delay in Interferometric Synthetic Aperture Radar Estimated from Meteorological Model and Multispectral Imagery." *Journal of Geophysical Research: Solid Earth* 112 (B5). doi:10.1029/2006JB004352.

Rosen, P. A., S. Hensley, G. Peltzer, and M. Simons. 2004. "Updated Repeat Orbit Interferometry Package Released." *Eos, Transactions American Geophysical Union* 85 (5): 47–47. doi:10.1029/2004EO050004.

Skamarock, W., J. Klemp, J. Dudhia, D. Gill, D. Barker, M. Duda, X. Huang, W. Wang, and J. Powers. 2008. "A Description of the Advanced Research WRF Version 3." NCAR technical note NCAR/TN/u2013475+ STR.

Talagrand, O. 1997. "Assimilation of Observations, an Introduction." *Journal of the Meteorological Society of Japan* 75 (1B): 191–209.

Wadge, G., P. Webley, I. James, R. Bingley, A. Dodson, S. Waugh, T. Veneboer, G. Puglisi, M. Mattia, and D. Baker. 2002. "Atmospheric Models, GPS and InSAR Measurements of the Tropospheric Water Vapour Field over Mount Etna." *Geophysical Research Letters* 29 (19): 11-1–11-4. doi:10.1029/2002GL015159.

Wadge, G., M. Zhu, R. Holley, I. James, P. Clark, C. Wang, and M. Woodage. 2010. "Correction of Atmospheric Delay Effects in Radar Interferometry Using a Nested Mesoscale Atmospheric Model." *Journal of Applied Geophysics* 72 (2): 141–149. doi:10.1016/j.jappgeo.2010.08.005.

Williams, S., Y. Bock, and P. Fang. 1998. "Integrated Satellite Interferometry: Tropospheric Noise, GPS Estimates and Implications for Interferometric Synthetic Aperture Radar Products." *Journal of Geophysical Research: Solid Earth* 103 (B11): 27051–27067.

Zebker, H. A., P. A. Rosen, and S. Hensley. 1997. "Atmospheric Effects in Interferometric Synthetic Aperture Radar Surface Deformation and Topographic Maps." *Journal of Geophysical Research* 102 (B4): 7547–7563.

Zeng, Q., Y. Li, and X. Li. 2007. "Correction of Tropospheric Water Vapour Effect on ASAR Interferogram Using Synchronous MERIS Data." In *IGARSS 2007 International Geoscience and Remote Sensing Symposium*, Barcelona, July 23–28.

Zhang, F., M. Zhang, and J. Poterjoy. 2013. "E3dvar: Coupling an Ensemble Kalman Filter with Three-Dimensional Variational Data Assimilation in a Limited-Area Weather Prediction Model and Comparison to E4dvar." *Monthly Weather Review* 141 (3): 900–917. doi:10.1175/MWR-D-12-00075.1.

Zhang, M., and F. Zhang. 2012. "E4dvar: Coupling an Ensemble Kalman Filter with Four-Dimensional Variational Data Assimilation in a Limited-Area Weather Prediction Model." *Monthly Weather Review* 140 (2): 587–600. doi:10.1175/MWR-D-11-00023.1.